Zero-dimensional Cuprous halide Scintillator with ultra-high anti-water stability for X-ray Imaging

Jing-Ning Lv[a†], Na Lin[a,b†], Jia-Yi Zhang[a], Yu-Meng Liu[a], Li-Chuang Niu[a], Jie Shi[a], Xiao-Wu Lei[a]*, Zhi-Wei Chen[a]*

[a] Research Institute of Optoelectronic Functional Materials, School of Chemistry, Chemical Engineering and Materials, Jining University, Qufu, Shandong, 273155, P. R. China

[b] School of Chemistry and Chemical Engineering, Qufu Normal University, Qufu, Shandong, 273165, P. R. China

[†] These authors contributed equally to this work.

Corresponding author: Xiao-Wu Lei; Zhi-Wei Chen

E-mail address: xwlei_jnu@163.com; zw_chen@jnxy.edu.cn

Experimental Section

Materials

All chemicals used in the reactions were commercially available and used directly without further purification. CuBr (99.9%), Ethoxycarbonylmethyl(triphenyl)phosphonium Bromide ($C_{22}H_{22}BrO_2P$, CEOM-TPPBr, 98%), Ethanol (≥99.5%), 1-Butanol (99.9%), hydrobromic acid (40%) and aqueous hypophosphoric acid (50%) were purchased from Aladdin.

Preparation of the $[CEOM\text{-}TPP]_2Cu_4Br_6$:

The $[CEOM\text{-}TPP]_2Cu_4Br_6$ single crystals was synthesized by volatilization method at room temperature. A mixture of CuBr (0.70 mmol, 0.10g) and CEOM-TPPBr (0.35 mmol, 0.15 g) was dissolved in ethanol (4 mL), 1-Butanol (2 mL), hydrobromic acid (1 mL) and hypophosphoric acid (1 mL). The mixture was stirred until the solution became clear and transparent. Subsequently, the clarified and transparent solution was left to naturally cool to room temperature, allowing the growth of the single crystals. After 5 days, the single crystals were filtered out and washed three times with ethanol, and dried naturally.

Fabrication of $[CEOM\text{-}TPP]_2Cu_4Br_6$@EVA Film:

2.0 g EVA was completely dissolved in cyclohexane (5 mL) to form solution under stirring at 60 °C for 1 h. Then, $[CEOM\text{-}TPP]_2Cu_4Br_6$ dispersed in 1 mL ethanol was added into the above solution under stirring until the formation of homogeneous and viscous fluid. The final flexible film was prepared by facilely coating on a glass and evaporated slowly in the ventilation cabinet at room temperature.

Stability test:

The anti-water stability was carried out by immersing the sample in deionized water. The acid stability was carried out by immersing the sample in acidic aqueous solution prepared from concentrated hydrochloric acid, while the base stability was carried out by immersing the sample in alkaline aqueous solution prepared from concentrated ammonium hydroxide.

Theoretical Calculation:

The electronic band structures and density of states (DOS) were theoretically calculated by using the first-principles plane-wave pseudopotential method with the code CASTEP provided by the software Materials Studio v7.0. Valence electrons were represented by C-$2s^2 2p^2$, N-$2s^2 2p^3$, O-$2s^2 2p^4$, P-$3s^2 3p^3$, Cu-$3d^{10} 4s^1$ and Br-$4s^2 4p^5$

orbitals. The other calculating parameters and convergent criteria were set the default values of the CASTEP code.

X-Ray Crystallography:

The single-crystal X-ray diffraction data of $[CEOM\text{-}TPP]_2Cu_4Br_6$ was collected on a Bruker Apex II CCD diffractometer with Mo-Ka radiation (λ = 0.71073 Å) room temperature. The crystal structures were solved and refined by using the SHELXL-2018/3 program within OLEX2, with all atoms being refined with anisotropic atomic displacement parameters, except the H atoms, which were placed in idealized positions and allowed to ride on the relevant carbon atoms. The crystal refinement parameters, bond angles, and bond lengths of compounds $[CEOM\text{-}TPP]_2Cu_4Br_6$ are listed in Tables S1-S4 in supporting information.

Common Characterizations:

The powder X-ray diffraction (PXRD) analysis was performed on Bruker D8 ADVANCE powder X-ray diffractometer equipped with Cu-*Kα* radiation at a voltage of 40 kV and a current of 40 mA. The diffraction patterns were scanned over the angular range of 5-60° (2*θ*) with a step size of 5 °/min at room temperature. The UV-vis absorption was measured directly on ground single crystals with BaSO4 as substrate in the wavelength range of 200-800 nm on PE Lambda 900 UV/vis spectrophotometer. The thermogravimetry analysis (TGA) was investigated on a Mettler TGA/SDTA 851 thermal analyzer under a N_2 atmosphere with a heating rate of 10 °C min^{-1} from 25 to 800 °C. The PL spectrum was performed on an Edinburgh FLS980 fluorescence spectrometer. The photoluminescence quantum yield (PLQY) was achieved by incorporating an integrating sphere into the FLS980 spectrofluorometer. The PLQY was calculated based on the equation: $\eta_{QE} = I_S/(E_R\text{-}E_S)$, in which I_S represents the luminescence emission spectrum of the sample, E_R was the spectrum of the excitation light from the empty integrated sphere (without the sample), and E_S was the excitation spectrum for exciting the sample. The time-resolved decay data was carried out using the Edinburgh FLS980 fluorescence spectrometer with a picosecond pulsed diode laser. The average lifetime was obtained by exponential fitting according to the following function:

$$I_{(t)} = I_0 + A_1 exp(\frac{-t}{\tau_1}) + A_2 exp(\frac{-t}{\tau_2})$$

where I is the emission intensity, t is the time after excitation, and τ is the lifetime of

the exponential component.

The corresponding Commission Internationale Eclairage (CIE) chromaticity coordinates were calculated based on the PL emission spectrum.

X-Ray Property Characterization:

RL spectrum was obtained using a 1000 fluorescence spectrometer (AMPTEK 0X tube) equipped with an X-ray source. The X-ray response intensity was detected and collected with Hamamatsu R928 PMT. Herein, the commercially available LuAG:Ce was used as a reference with known light yield of about 22000 photon/MeV. The $[CEOMTPP]_2Cu_4Br_6$ crystal was ground into fine powder and pressed in to a round piece with 1 cm diameter and 1 mm thickness, which was the same as standard reference of LuAG:Ce. The 0D hybrid Cu halides and LuAG:Ce scintillators were set at the same position to unify the radiation dose and field in RL spectral measurement. Light yield was defined as the ratio of photon numbers emitted from the luminescent sites to the total absorbed X-ray energy, it represents an internal X-ray conversion efficiency. Therefore, the emission photon counts of scintillators were normalized to the same X-ray attenuation. Furthermore, the spectral corrections (e.g., sensibility, wavelength and absorption coefficience) were also considered for the scintillation yield calculation. By comparing corrected response amplitude (R) of LuAG:Ce and samples, the light yield can be estimated by the following formula:

$$\frac{LY_{sample}}{LY_{LuAG:Ce}} = \frac{R_{sample}}{R_{LuAG:Ce}} \times \frac{\int I_{LuAG:Ce}(\lambda)/S(\lambda) \int I_{LuAG:Ce}(\lambda)d\lambda}{\int I_{sample}(\lambda)/S(\lambda) \int I_{sample}(\lambda)d\lambda}$$

where R is defined as the X-ray deposited energy percentage of scintillators, $I(\lambda)$ is the radioluminescence spectrum at different wavelengths, and $S(\lambda)$ represents the detection efficiency at different irradiation area, respectively. The absorption coefficient (α) for X-ray was mainly determined by the effective atomic number (Z_{eff}) as $\alpha \propto \rho Z_{\text{eff}}^4/E^3$, where ρ is the mass density and E is the X-ray photon energy. The X-ray detection was carried out under irradiation with X-rays at 120 kVp. The operating current of the X-ray tube was tuned to 50 mA. The radiation dose rate was calibrated with a commercial dosimeter from Germany (IBA, MagicMax Universal, XR Multidetector). A Mini-X X-ray tube was utilized as the X-ray source, generating an X-ray output spectrum with both intense characteristic radiation of Ag and broad bremsstrahlung radiation. The average

X-ray photon energy was ~22 keV. The X-ray dose rates were calibrated by a highly sensitive X-ray ion chamber dose meter (Radcal Corporation 10 × 5-180). The objects and scintillator wafers were placed vertically to the incident X-rays, and the scintillators were fixed just behind the objects. A reflector was utilized to deflect the optical path by 90° to diminish the negative influence caused by direct radiation from the X-ray source on the camera.

Calculation of Detection limit:

The linear relationship between the RL intensity and X-ray dose under low dose rate was obtained. The noise data was obtained in the absence of sample. The noise intensity values were statistically analyzed by fitting a Gaussian function with FWHM as the average of the noise. The detection limit of dose rate was obtained from the slope of the fitting line when the signal-to-noise ratio equal to 3.

X-Ray imaging:

To collect X-ray images, a CMOS camera was equipped. The camera (CMOS camera Photometrics 95B) has an active area of 13.3 mm × 13.3 mm, with a 2048 × 2048 pixel grid (6.5 μm × 6.5 μm each).

Calculation of MTF:

The MTF profile is calculated by the beveled edge method. First, a piece of aluminum with a sharp edge (thickness: about 1 mm) is placed on the scintillator and its edge profile is derived from the generated X-ray image. Then, the edge diffusion function (ESF) is derived from the edge profile, from which we can derive the line diffusion function (LSF). Finally, the MTF value is defined by the Fourier transform of the LSF as follows:

$$\mathrm{MTF}(v) = F\left(\mathrm{LSF}(x)\right) = F\left(\frac{d\mathrm{ESF}(x)}{dx}\right)$$

where v is the spatial frequency, and x is the position of the pixels.

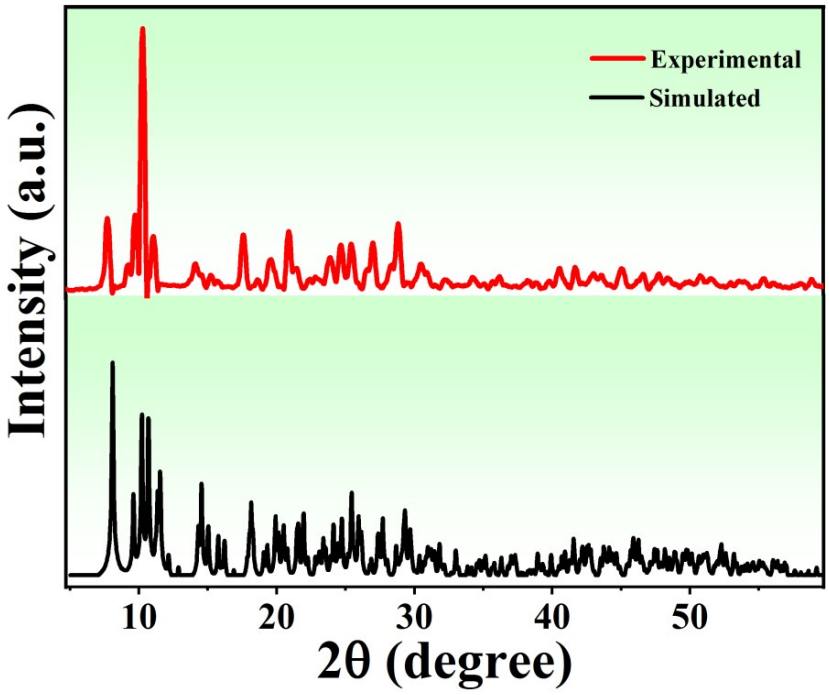

Fig. S1. Simulated and experimental XRD patterns of $[CEOMTPP]_2Cu_4Br_6$.

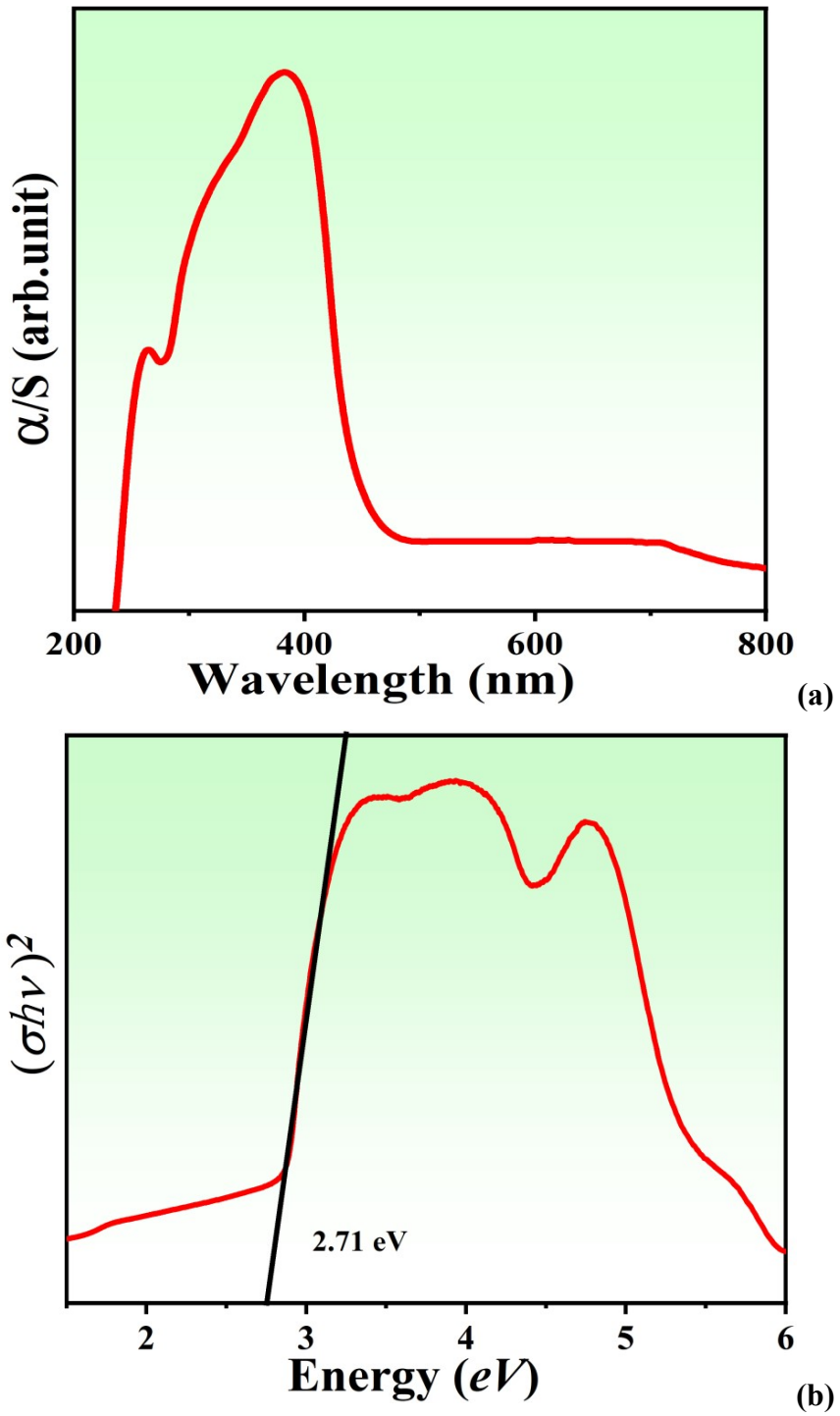

Fig. S2. (a) The solid state UV-vis adsorption spectrum and (b) the Tauc plot for direct band gap of $[CEOM\text{-}TPP]_2Cu_4Br_6$.

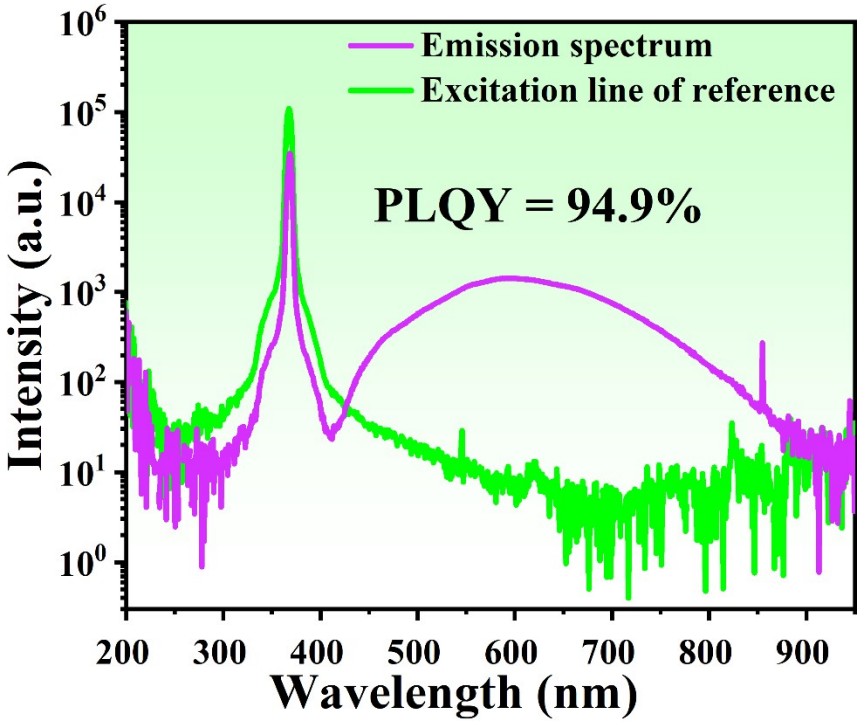

Fig. S3. The PLQY of $[CEOM\text{-}TPP]_2Cu_4Br_6$.

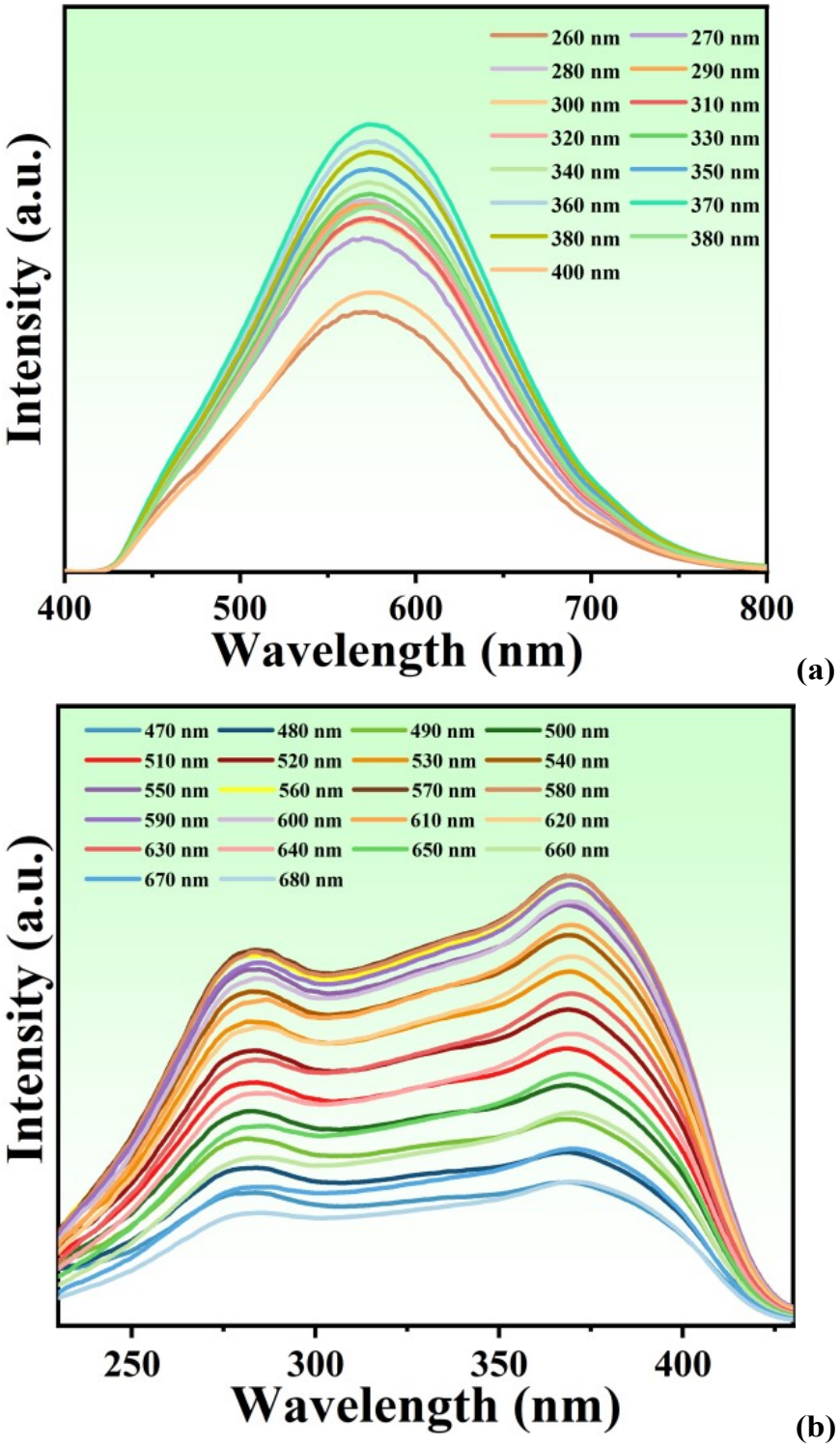

Fig. S4. (a) The excitation wavelength dependent PL emission spectra; (b) The emission wavelength dependent PL excitation spectra.

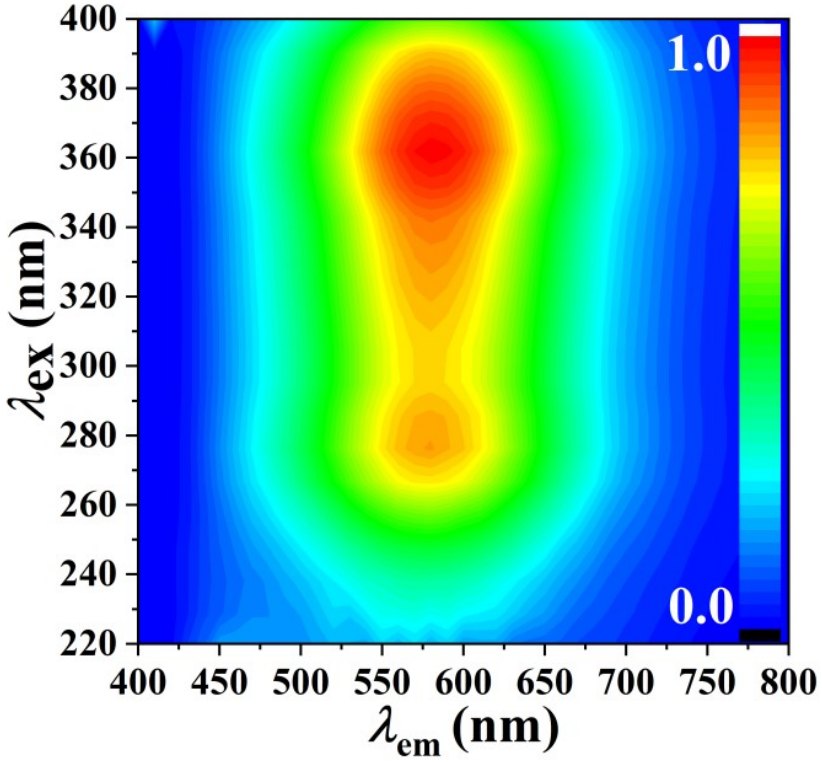

Fig. S5. 3D consecutive PL excitation and emission correlation map of [CEOM-TPP]$_2$Cu$_4$Br$_6$.

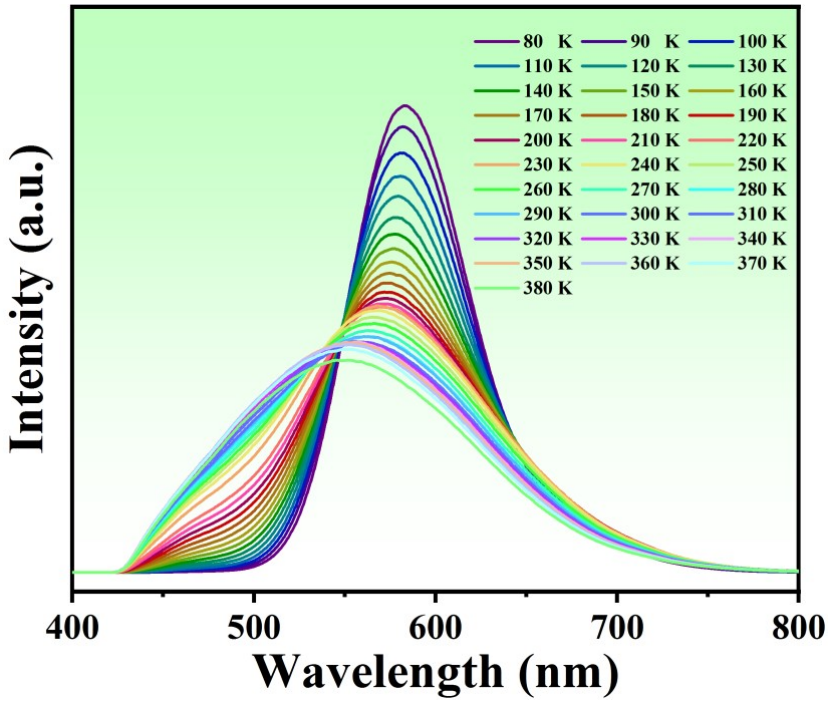

Fig. S6. The PL emission spectrum at different temperature from 80 K to 380 K.

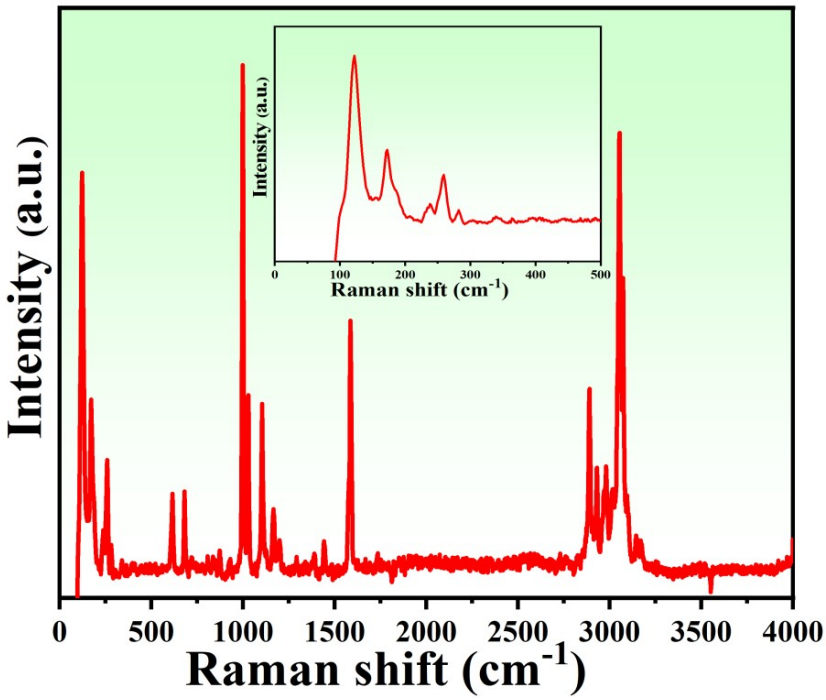

Fig. S7. The Raman spectrum of $[CEOM\text{-}TPP]_2Cu_4Br_6$.

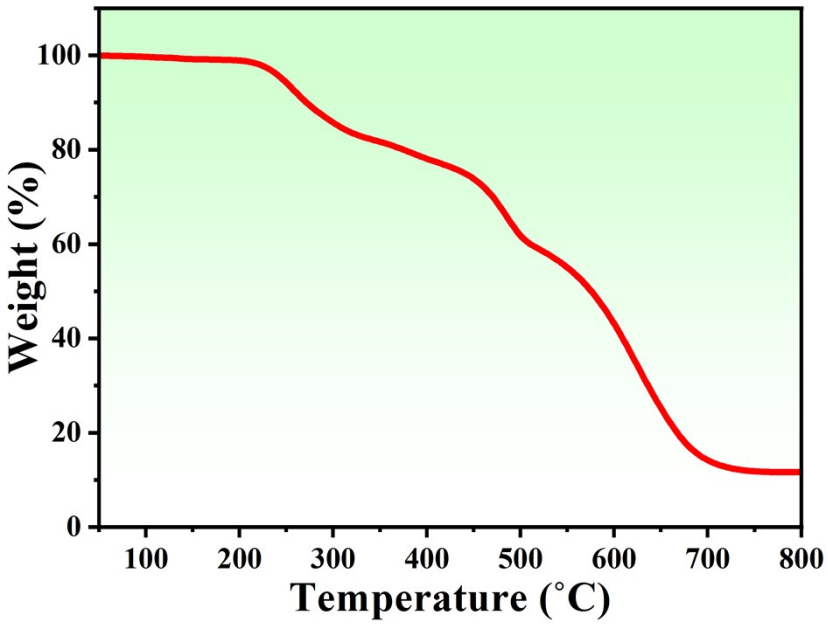

Fig. S8. The thermogravimetric analyses (TGA) curve for $[CEOM\text{-}TPP]_2Cu_4Br_6$.

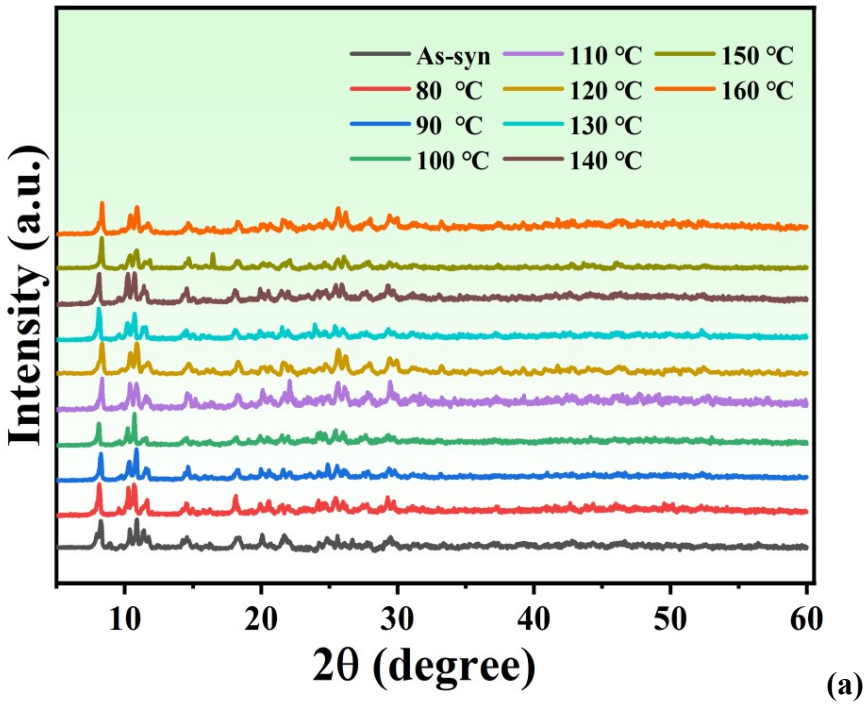

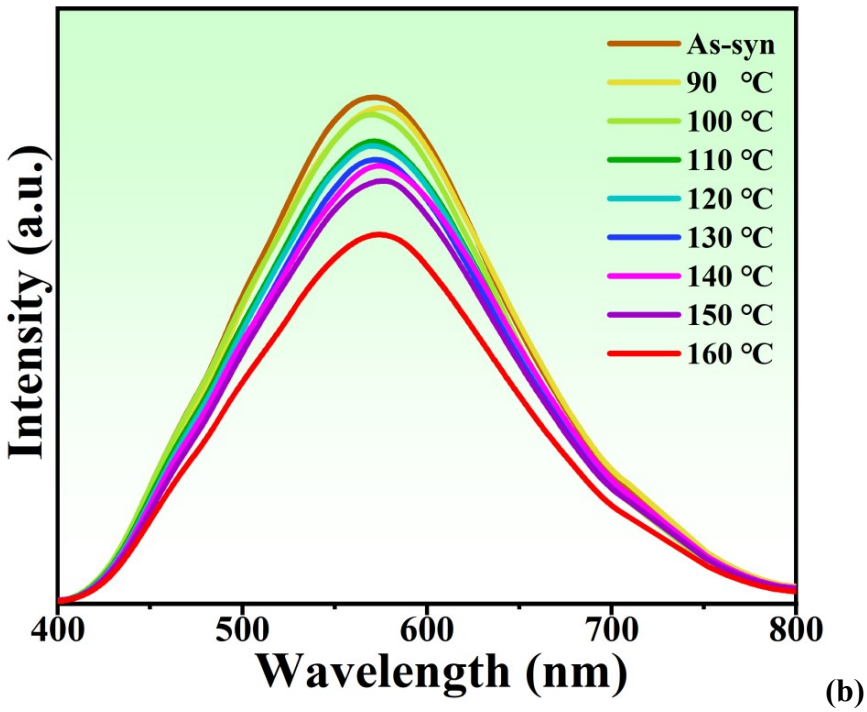

Fig. S9. (a) The PXRD patterns and (b) PL emission spectra of $[CEOM\text{-}TPP]_2Cu_4Br_6$ after continuous heating at different temperature.

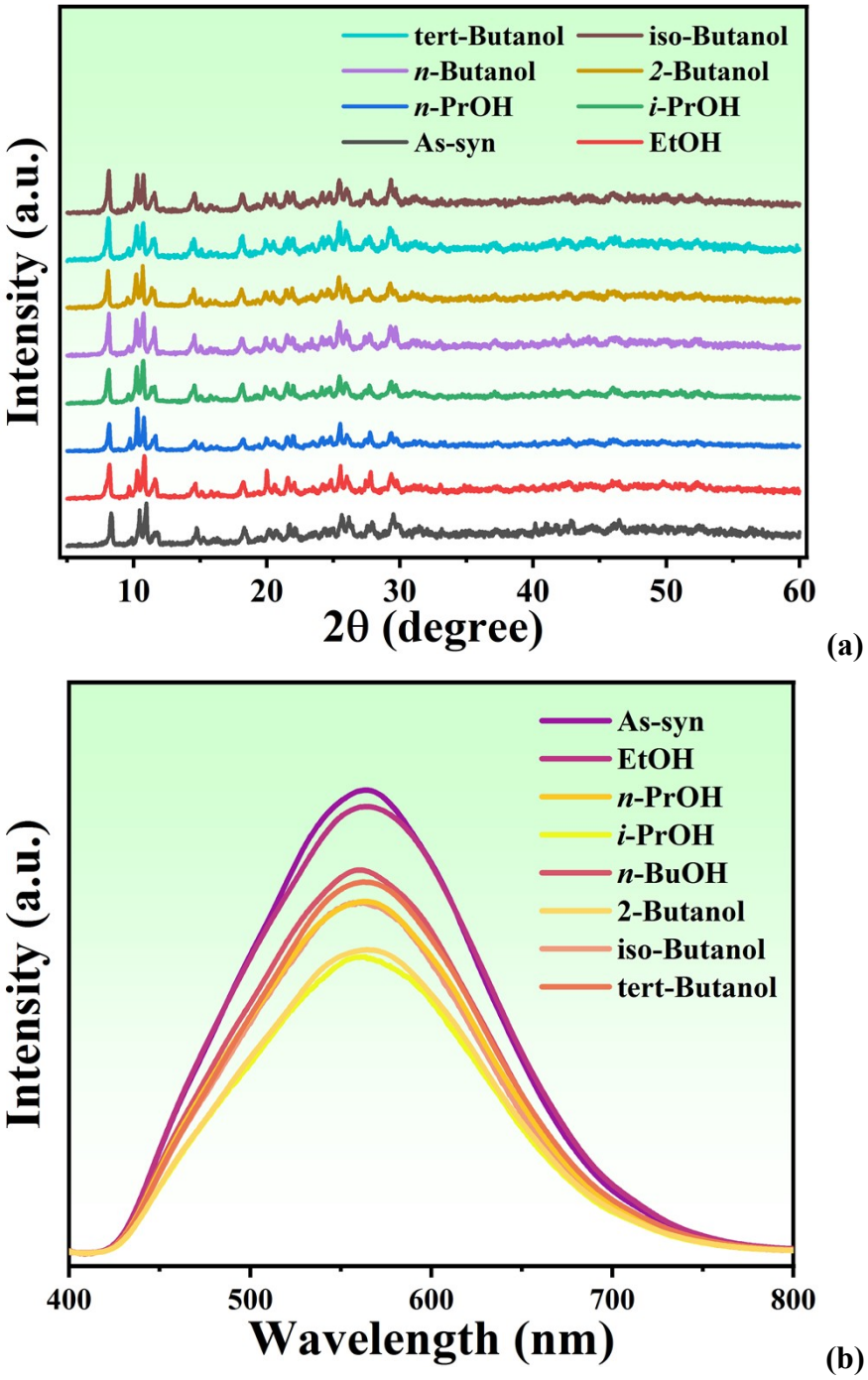

Fig. S10. (a) The PXRD and (b) PL emission spectra of $[CEOM\text{-}TPP]_2Cu_4Br_6$ after soaking in various organic solutions over one day.

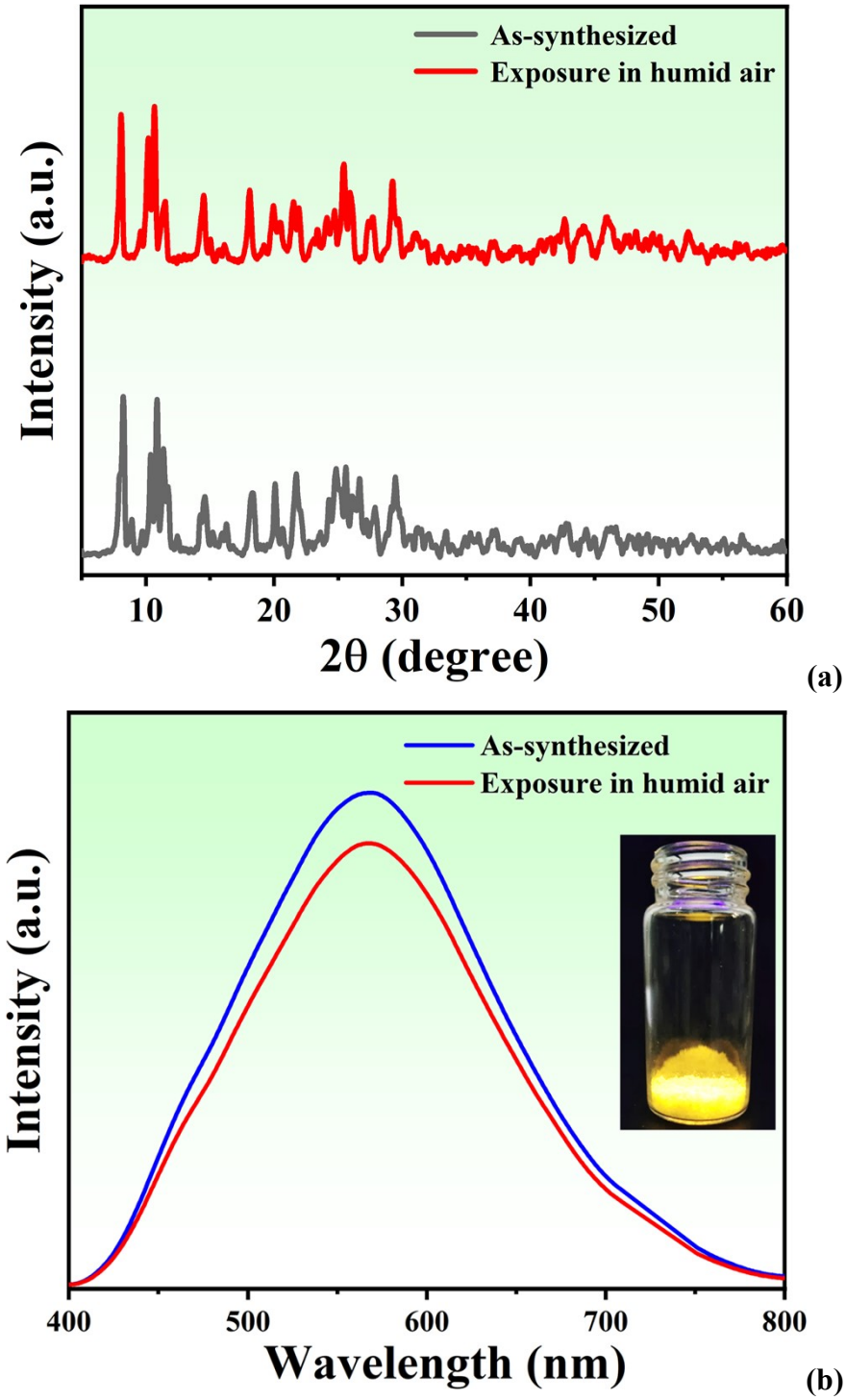

Fig. S11. (a) The PXRD and (b) PL emission spectra of $[CEOM\text{-}TPP]_2Cu_4Br_6$ after exposure in humid air over one year (Insert show the photographs of the sample exposure in humid air for one year under UV light).

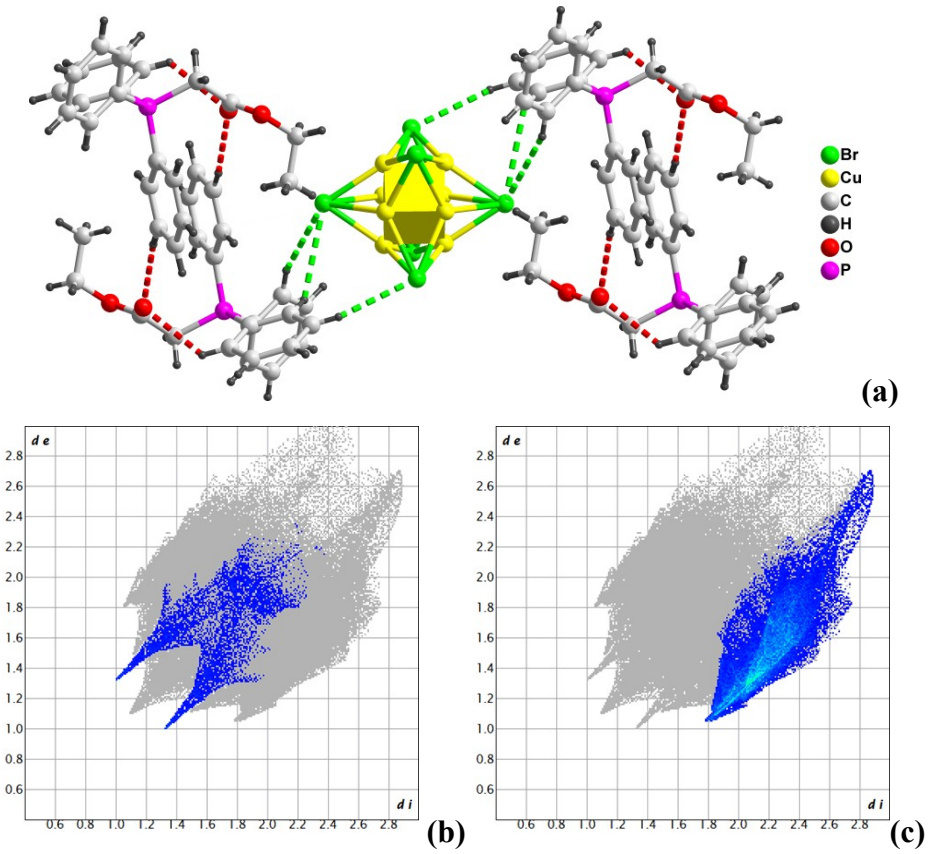

Fig. S12. (a) Details for hydrogen bonding in $[CEOMTPP]_2Cu_4Br_6$. The 2D fingerprint plot about (b) O···H and (c) Br···H of $[CEOMTPP]_2Cu_4Br_6$ obtained from Hirshfeld surface calculations.

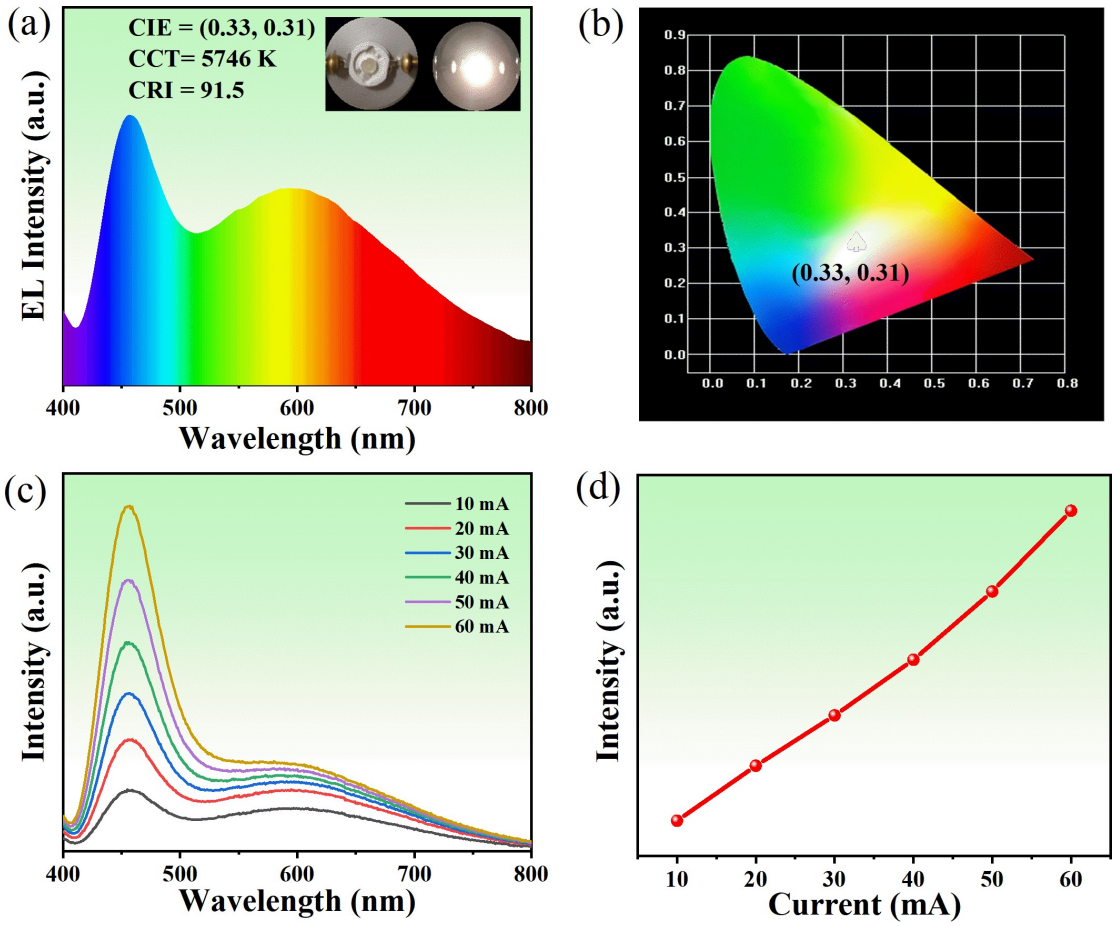

Fig. S13. (a) PL emission spectrum of fabricated white LED under drive of 10 mA current. (b) CIE coordinates of fabricated LED. (c) PL emission spectra of fabricated white LED under varied current from 10 to 60 mA. (d) The normalized PL intensity depend on different drive current from 10 mA to 60 mA.

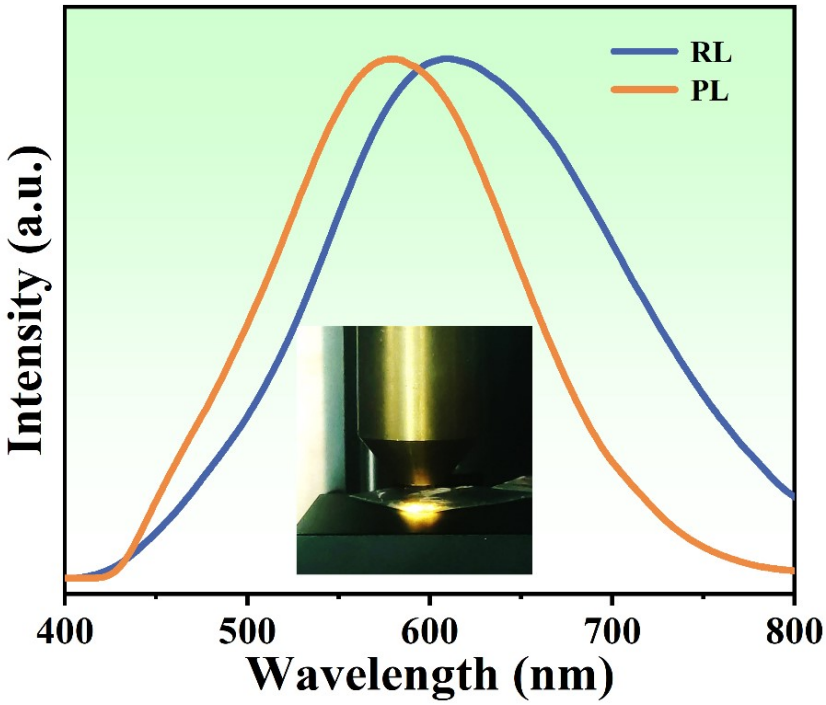

Fig. S14. The comparison of RL and PL spectra for $[CEOM\text{-}TPP]_2Cu_4Br_6$.

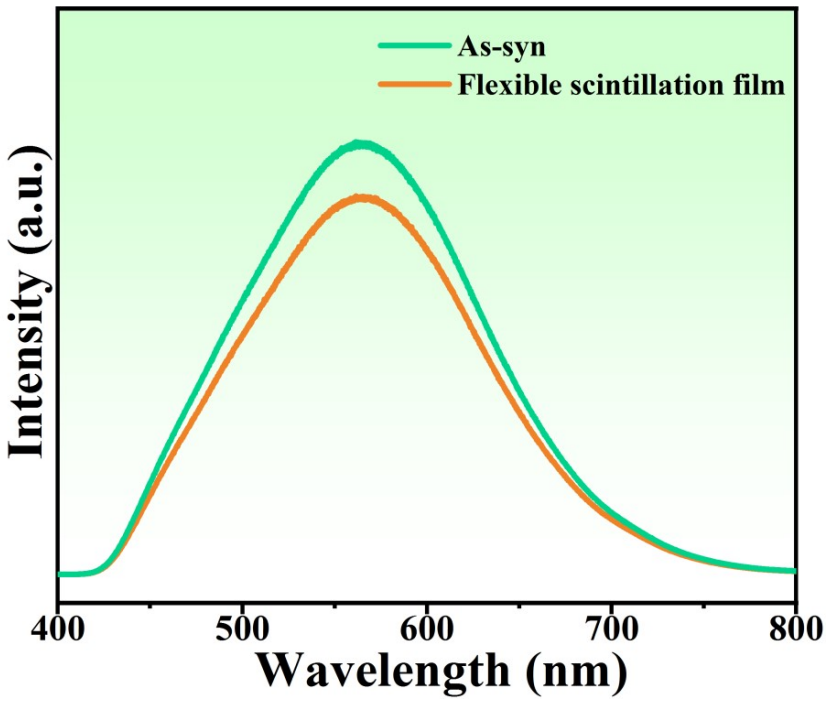

Fig. S15. The comparison of PL spectra for $[CEOM\text{-}TPP]_2Cu_4Br_6$ crystals and the flexible scintillation film.

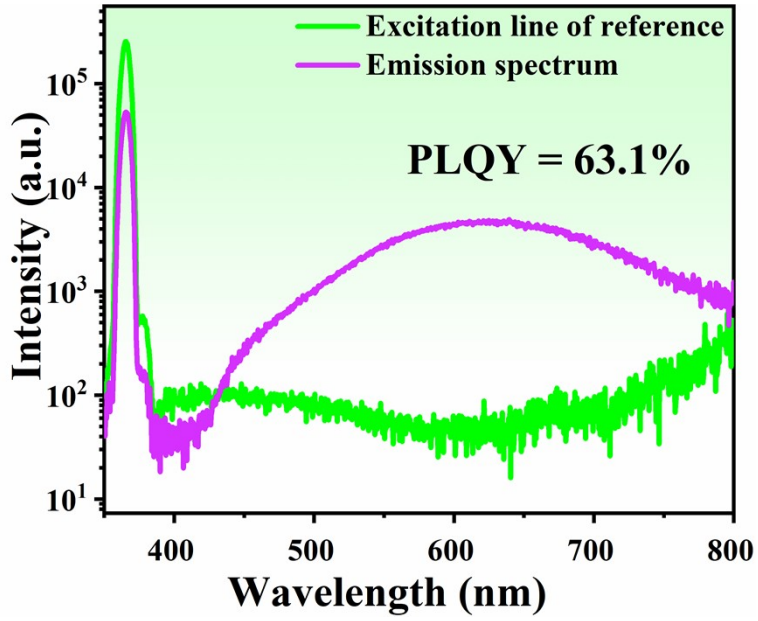

Fig. S16. The PLQY of $[CEOM\text{-}TPP]_2Cu_4Br_6$@EVA film.

Table S1. Crystal Data and Structural Refinements for $[CEOMTPP]_2Cu_4Br_6$.

Compound	$[CEOM\text{-}TPP]_2Cu_4Br_6$
chemical formula	$C_{22}PH_{22}O_2Cu_2Br_3$
FW	716.17
Space group	$P2_1/n$
a/Å	10.5589(5)
bÅ	15.3185(7)
c/Å	15.6841(7)
α/°	90
β/°	96.628(2)
γ/°	90
V(Å^3)	2519.9(2)
Dcalcd (g·cm^{-3})	1.888
Temp (K)	273.15
μ (mm^{-1})	6.524
F (000)	1392.0
Reflections collected	32277
Unique reflections	4449
GOF on F^2	1.002
[a]R_1,wR_2 ($I > 2\sigma(I)$)	0.0388/0.0674
[b]R_1,wR_2 (all data)	0.0807/0.0798

[a]$R_1 = \sum||F_o| - |F_c||/\sum|F_o|$. [b]$wR_2 = [\sum w(F_o^2 - F_c^2)^2/\sum w(F_o^2)^2]^{1/2}$.

Table S2. Selected bond lengths (Å) in $[CEOMTPP]_2Cu_4Br_6$.

Br1-Cu1	2.3715(14)	Cu1-Cu2	1.9306(18)
Br1-Cu2	2.3434(14)	Cu1-Cu2$^{\#1}$	2.6735(17)
Br1-Cu3	2.4072(14)	Cu1-Cu3$^{\#1}$	1.9391(18)
Br1-Cu4	2.4012(15)	Cu1-Cu3	2.7280(18)
Br2-Cu1	2.3766(14)	Cu1-Cu4	1.8407(17)
Br2-Cu2	2.3971(13)	Cu1-Cu4$^{\#1}$	2.7821(18)
Br2-Cu3$^{\#1}$	2.3882(13)	Cu2-Cu3	1.8705(17)
Br2-Cu4$^{\#1}$	2.4375(14)	Cu2-Cu3$^{\#1}$	2.7750(18)
Br3-Cu1	2.4030(14)	Cu2-Cu4	2.6987(17)
Br3-Cu2$^{\#1}$	2.4164(14)	Cu2-Cu4$^{\#1}$	1.9604(18)
Br3-Cu3$^{\#1}$	2.3747(14)	Cu3-Cu4$^{\#1}$	2.7077(17)
Br3-Cu4	2.3817(15)	Cu3-Cu4	2.0302(18)

$^{\#1}$1-*x*, -*y*, 1-*z*.

Table S3. Selected bond angles (°) in $[CEOMTPP]_2Cu_4Br_6$

Cu1-Br1-Cu3	69.62(4)	Br3-Cu1-Cu2$^{\#1}$	56.55(4)
Cu1-Br1-Cu4	45.37(4)	Br3-Cu1-Cu3	110.31(5)
Cu2-Br1-Cu1	48.34(5)	Br3-Cu1-Cu4$^{\#1}$	108.07(5)
Cu2-Br1-Cu3	46.35(4)	Cu2-Cu1-Br1	65.07(6)
Cu2-Br1-Cu4	69.32(4)	Cu2-Cu1-Br2	66.70(5)
Cu4-Br1-Cu3	49.95(4)	Cu2-Cu1-Br3	146.53(7)
Cu1-Br2-Cu2	47.71(4)	Cu2-Cu1-Cu2$^{\#1}$	89.99(6)
Cu1-Br2-Cu3$^{\#1}$	48.03(4)	Cu2-Cu1-Cu3$^{\#1}$	91.64(8)
Cu1-Br2-Cu4$^{\#1}$	70.59(4)	Cu2-Cu1-Cu3	43.26(5)
Cu2-Br2-Cu4$^{\#1}$	47.84(4)	Cu2^{1}-Cu1-Cu3	61.82(5)
Cu3^{1}-Br2-Cu2	70.89(4)	Cu2-Cu1-Cu4$^{\#1}$	44.79(5)
Cu3^{1}-Br2-Cu4$^{\#1}$	49.75(4)	Cu2^{1}-Cu1-Cu4$^{\#1}$	59.25(5)
Cu1-Br3-Cu21	67.38(4)	Cu3^{1}-Cu1-Br1	147.56(7)
Cu3^{1}-Br3-Cu1	47.89(4)	Cu3^{1}-Cu1-Br2	66.30(5)
Cu3^{1}-Br3-Cu2$^{\#1}$	45.95(4)	Cu3^{1}-Cu1-Br3	65.29(6)
Cu3^{1}-Br3-Cu4	69.40(4)	Cu3^{1}-Cu1-Cu2$^{\#1}$	44.39(5)
Cu4-Br3-Cu1	45.25(4)	Cu3^{1}-Cu1-Cu3	91.76(6)
Cu4-Br3-Cu2$^{\#1}$	48.23(4)	Cu3^{1}-Cu1-Cu4$^{\#1}$	46.86(5)
Br1-Cu1-Br2	118.21(6)	Cu3-Cu1-Cu4$^{\#1}$	58.86(5)
Br1-Cu1-Br3	122.75(6)	Cu4-Cu1-Br1	68.17(6)
Br1-Cu1-Cu2$^{\#1}$	110.06(5)	Cu4-Cu1-Br2	147.12(8)
Br1-Cu1-Cu3	55.81(4)	Cu4-Cu1-Br3	66.76(6)
Br1-Cu1-Cu4$^{\#1}$	106.45(6)	Cu4-Cu1-Cu2$^{\#1}$	47.16(6)
Br2-Cu1-Br3	118.89(6)	Cu4-Cu1-Cu2	91.35(8)
Br2-Cu1-Cu2$^{\#1}$	106.13(6)	Cu4-Cu1-Cu3$^{\#1}$	91.47(8)
Br2-Cu1-Cu3	106.15(6)	Cu4-Cu1-Cu3	48.09(6)
Br2-Cu1-Cu4$^{\#1}$	55.73(4)	Cu4-Cu1-Cu4$^{\#1}$	91.41(6)

$^{\#1}$1-*x*, -*y*, 1-*z*

Table S4. Hydrogen bonds data for $[CEOMTPP]_2Cu_4Br_6$.

D-H···A	d(D-H)	d(H···A)	d(D···A)	<(DHA)
C8-H8-Br1	0.93	3.22	3.919(5)	133.6
C9-H9-Br2$^{\#1}$	0.93	2.98	3.824(6)	152.4
C10-H10-Br1$^{\#2}$	0.93	3.08	3.964(6)	159.7
C12-H12-O2	0.93	2.52	3.171(6)	126.9
C14-H14-O1$^{\#3}$	0.93	3.01	3.570(6)	120.2
C15-H15-Br2$^{\#4}$	0.93	3.04	3.697(5)	129.1
C15-H15-O1$^{\#3}$	0.93	2.83	3.488(7)	128.3
C16-H16-Br2$^{\#4}$	0.93	3.08	3.716(5)	127.1
C17-H17-O2$^{\#5}$	0.93	2.47	3.357(6)	159.7
C19-H19B-Br3$^{\#6}$	0.97	2.98	3.939(5)	170.0

$^{\#1}$1-*x*, -*y*, 1-*z*; $^{\#2}$-1/2+*x*, 1/2-*y*, -1/2+*z*; $^{\#3}$2-*x*, 1-*y*, 1-*z*; $^{\#4}$3/2-*x*, 1/2+*y*, 3/2-*z*; $^{\#5}$1-*x*, 1-*y*, 1-*z*; $^{\#6}$3/2-*x*, 1/2+*y*, 1/2-*z*